Initial- and final-state effects in the conduction bands of $2H$-$MoS_2(0001)$ studied by $k_{\parallel}$-resolved inverse photoemission spectroscopy

V. Langlais, H. Belkhir, J.-M. Themlin, and J.-M. Debever
Groupe de Physique des Etats Condensés, Faculté des Sciences de Luminy, Case 901, F-13288 Marseille cedex 9, France

L.-M. Yu and P. A. Thiry
Institute for Studies in Interface Sciences, Facultés Universitaires Notre-Dame de la Paix, 61 rue de Bruxelles, B-5000 Namur, Belgium

(Received 25 May 1995)

The conduction-band structure of the lamellar semiconductor molybdenum disulfide $MoS_2(0001)$ has been studied by $k_{\parallel}$-resolved inverse photoemission spectroscopy (KRIPES) along two major symmetry directions ($\bar{M}'\bar{\Gamma}\bar{M}$ and $\bar{K}'\bar{\Gamma}\bar{K}$) of the surface Brillouin zone. Among the three observed features, the lowest-energy one (A) is attributed to antibonding combinations of Mo $4d$ and S $3p$ states. After decomposition, the experimental dispersion of its individual components is compared with theoretical band-structure calculations. An overall agreement is found with three calculations, except for a dispersionless shoulder observed just above the Fermi level near the $\bar{\Gamma}$ point. This peak is interpreted as resulting from a narrow impurity band. The relatively high intensity of the A features is explained by a resonant optical transition with initial states found at 9.5 eV above the Fermi level, which are also detected in the modulations of the target current. Moreover, from both KRIPES and target current measurements, the intensity of the various A components is observed to behave differently along the two equivalent but opposite azimuths $\bar{\Gamma}\bar{M}$ and $\bar{\Gamma}\bar{M}'$. This reflects the asymmetric atomic arrangement of MoS_2 in this direction.

I. INTRODUCTION

The lamellar transition metal dichalcogenides TX_2 are characterized by a two-dimensional crystal structure with strong chemical bonding in a quasi-two-dimensional sandwich-type layer and only weak interaction between the layers. The sandwich layers are formed by X-T-X repetition units, where X can be S, Se, and Te while T stands for a transition metal of the *IVB*, *VB*, or *VIB* group. There are three possible symmetries of the cleaved surfaces of these crystals: trigonal, hexagonal, and rhombohedral but different stacking sequences between the layers lead to different sizes for the unit cell indicated by a number n before the layer symmetry.[1] Due to their anisotropic optical, mechanical, and transport properties and intercalation possibilities, these lamellar compounds have been extensively studied with various experimental techniques.[2–12] Moreover, modern heteroepitaxial techniques, known as van der Waals epitaxy, use cleaved surfaces of such lamellar materials as starting substrates because their weak bonding favors the crystalline growth, even in the absence of a good lattice match between substrate and adsorbate.[13]

Among the TX_2 family, $2H$-MoS_2 is a semiconductor where each molybdenum atom links to six sulfurs with covalent prismatic trigonal bonding [Fig. 1(a)]. $2H$ means that the symmetry of each layer is hexagonal and that the unit cell contains two sandwich layers of S-Mo-S rotated by 60° and translated with respect to one another is shown in Fig. 1(b). The crystal symmetry belongs to the D_{6h}^4 space group and the three-dimensional Brillouin zone (BZ) is shown in Fig. 1(c). From band-structure calculations, it follows that the top of the valence band is situated at Γ and that the bottom of the conduction band is reached halfway between Γ and the K point. The experimental value of the indirect band gap is 1.2 eV.[3] Recently, the valence-band dispersion of $2H$-MoS_2 has been measured by angle-resolved photoemission spectroscopy[4] (ARPES) in both directions parallel and perpendicular to the basal plane. This result has been used to test the occupied band structure of the material as predicted by different theoretical approaches[1,2,14–19] reviewed by

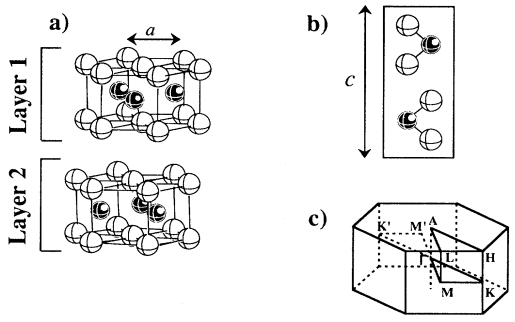

FIG. 1. Schematic drawing of the MoS_2 crystal showing (a) the trigonal prismatic coordination of the molybdenum atom linked to six sulfurs with $a = 3.160$ Å and $c = 12.294$ Å as structure parameters (Ref. 1); (b) [110] cross section of the hexagonal unit cell (Ref. 2); (c) first Brillouin zone of a hexagonal Bravais lattice.

several authors.[15,20] The best agreement was found when a self-consistent approach was used. On the other hand, one single angle-integrated experiment has been reported on the unoccupied band structure.[9]

In this paper, we reported on $k_{\parallel}$-resolved inverse photoemission spectroscopy (KRIPES) and target current spectroscopy (TCS) measurements of the conduction-band dispersion of $2H$-MoS_2 along two major symmetry directions. The results will be compared with three theoretical predictions. With the combination of KRIPES and TCS, a resonant optical transition is found for the higher intensity of the lowest-energy band observed in the photon spectra. An asymmetric intensity ratio is clearly observed in the $\bar{M}'\bar{\Gamma}\bar{M}$ direction which is related to the structure of the material.

II. EXPERIMENT

The experiments have been performed in an UHV chamber (base pressure 10^{-10} Torr) equipped with a low-energy electron diffractometer (LEED) and the inverse photoemission system consisting of a BaO electron gun and an elliptical mirror to focus photons emitted in a large solid angle towards a Geiger-Müller photon counter. Together with its SrF_2 high-pass window, this detector operates at an isochromatic energy of 9.5 eV. The global energy resolution of this system is about 350 meV while the angular resolution is defined by the dispersion of the electron beam which is about 3° in the optimal conditions. More details about this spectrometer have been given elsewhere.[21] A KRIPES spectrum is obtained by scanning the kinetic energy of the incident electron at a certain polar angle θ. The $k_{\parallel}$-dependent band features are investigated by rotating the electron gun in a vertical plane perpendicular to the sample from either side of the surface normal along high symmetry directions within the surface planes associated with ΓALM and ΓAHK [see Fig. 1(c)] of the Brillouin zone. In that configuration, $\bar{\Gamma}\bar{M}$ ($\bar{\Gamma}\bar{K}$) and $\bar{\Gamma}\bar{M}'$ ($\bar{\Gamma}\bar{K}'$) correspond to opposite azimuths of the same direction of the surface BZ, scanned, respectively, by positive and negative angles of rotation of the electron gun.

A basal surface was obtained by covering the surface of a natural $2H$-MoS_2 single crystal with an adhesive tape and stripping it inside an introduction chamber under a pressure of 10^{-8} Torr. The sample was then immediately transferred *in vacuo* to the analysis chamber where the base pressure was 10^{-10} Torr. Such a low pressure allows ample time for the KRIPES measurements on this very inert surface. A sharp hexagonal LEED pattern was observed. As the sample was mounted on a rotating holder, the azimuth ϕ can be adjusted manually to align the two main directions into the plane of incidence of the electron beam. We point out that the accuracy of the azimuth alignment is also limited by the roughness of the surface obtained from the above-described cleavage procedure. The energy reference of the KRIPES spectra was set at the Fermi level and measured from the cutoff of the emission from a clean tantalum foil, which was in good electric contact with the sample.

III. RESULTS AND DISCUSSION

A. Experimental conduction-band dispersion

Figure 2 shows the KRIPES spectra recorded in the $\bar{\Gamma}\bar{M}$ and $\bar{\Gamma}\bar{M}'$ directions from both sides of the surface normal. The intensities have been normalized to the transmitted sample current. The experimental data are presented with dots while the corresponding solid lines are obtained by the sum of a linear background and a set of Gaussians. One example of such a set is plotted at the bottom of Fig. 2. Only the significant peaks are marked and will be considered in the later discussion, while the others are only used to fill the whole energy range. The number of Gaussians is kept constant in all the fitting procedure and their widths are smaller than 1 eV.

Three distinct features are seen in Fig. 2.

(1) The higher-energy feature (C) only appears near the $\bar{\Gamma}$ point. It splits into two peaks for $\theta=\pm 5°$ and disappears after 10°.

(2) A nondispersive peak (B) appears at 6 eV around $\theta=-30°$ but it is less significant on the other side of positive angles (see left panel of Fig. 2).

(3) Most of the observed photons are concentrated in the lower-energy feature (A). It starts with a sharp peak (A_2) with two shoulders (labeled as A_1, A_3) sitting on both sides. A_1 reaches its maximum intensity near the zone boundary. A_2 always remains dominant over the whole BZ and starts to split into A_2 and A_2' around $\theta=\pm 15°$, where A_3 disappears. A large dispersion of the

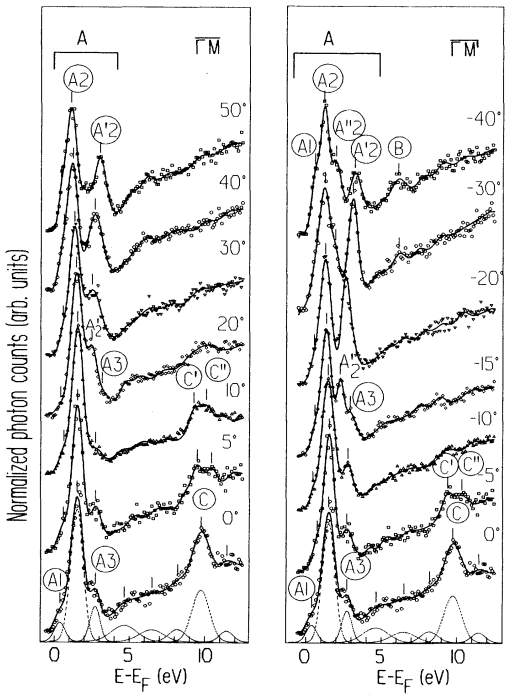

FIG. 2. Inverse photoemission spectra recorded in the $\bar{\Gamma}\bar{M}$ (positive angles) and $\bar{\Gamma}\bar{M}'$ (negative angles) directions. A typical fitting with a set of Gaussians after linear background subtraction is shown for the experimental spectrum at $\theta=0°$. The intensities are normalized to the target current.

order of 1.5 eV is clearly observed for the band A_2'. A shoulder splits out again from A_2 around $\theta=-30°$, which is labeled as A_2''. This latter splitting is not so clearly observed on the other side.

The KRIPES spectra recorded in the $\bar{K}'\bar{\Gamma}\bar{K}$ direction are plotted in Fig. 3. Similarly to the $\bar{M}'\bar{\Gamma}\bar{M}$ direction, three features can be distinguished: (1) peak C appears near the BZ center but it does not seem split in this case; (2) peak B comes out after $\theta=-30°$ but is essentially significant for the negative polar angles as observed in the $\bar{M}'\bar{\Gamma}\bar{M}$ direction; and (3) for the lowest-energy feature (A), four bands can be tracked. As a shoulder sitting at the lowest energy of the conduction band, the intensity of A_1 reaches its maximum at $\theta=\pm30°$ corresponding to the middle of $\bar{\Gamma}\bar{K}$. As in the $\bar{\Gamma}\bar{M}$ direction, two split structures originating from A_2 are visible. The first one (A_2') emerges around 12.5° on both sides and its intensity increases very fast until 40° where the second splitting (A_2'') occurs. The origin of this second structure is not clear as it seems to stem from A_2' for the positive polar angles, but from A_2 for the negative ones. In any case, its energy dispersion is almost symmetric with respect to $\bar{\Gamma}$.

Let us point out that KRIPES measurements are affected by the distribution of the initial states involved in the radiative transitions of the incident electrons. If the initial states are uniformly distributed in the $(E,k_\parallel)$ plane, the KRIPES spectra will reflect the density of the final states over the whole BZ. On the contrary, structures in the initial-state density will affect the KRIPES peak intensities and emphasize particular points of the conduction bands. For the band mapping, we will mainly concentrate on the lowest-energy feature A, for which calculations are available. With the peak positions (E_f) determined by the above-described fitting procedure, and considering that because of the presence of the surface, the electron momentum is conserved only for the component parallel to the surface ($k_\parallel$), we obtain the following equation:

$$|\mathbf{k}_\parallel|=\left[\left(\frac{2m}{\hbar^2}\right)(E_f+\hbar\omega-\phi_s)\right]^{1/2}\sin\theta\ , \tag{1}$$

where θ is the angle of incidence of the electron beam, m is the free electron mass, E_f the energy of the final state referenced to the Fermi level, $\hbar\omega$ the photon energy, and ϕ_s the sample work function, which is 4.9 eV for 2H-MoS_2.[11] The experimental bands are plotted in Fig. 4 for the $\bar{M}'\bar{\Gamma}\bar{M}$ and $\bar{K}'\bar{\Gamma}\bar{K}$ directions, respectively, where the full dots correspond to well-resolved peaks while the open dots represent shoulders, whose positions are less accurate. Five individual branches (labeled as A_1, A_2, A_2', A_2'', and A_3) which are symmetrically distributed on both sides of the BZ can be distinguished. The lower-lying branch A_1 is almost flat for both directions, while A_3 is only observed near the $\bar{\Gamma}$ point in the $\bar{M}'\bar{\Gamma}\bar{M}$ direction. From the BZ center, a degenerated peak A_2 splits into three branches: A_2, A_2', and A_2''.

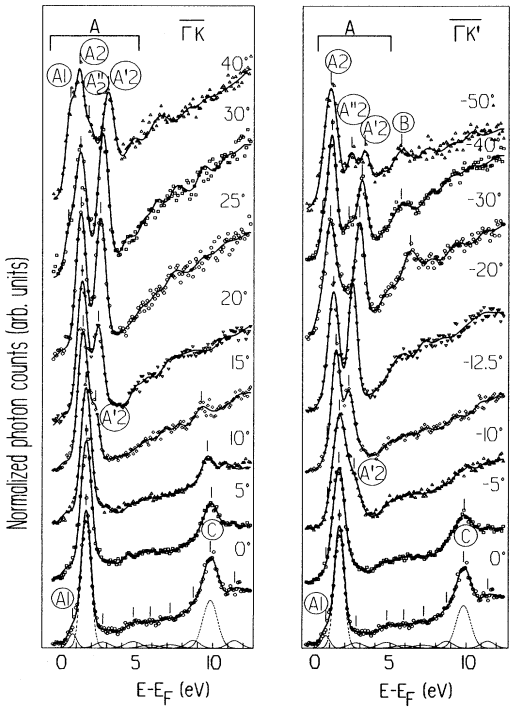

FIG. 3. Inverse photoemission spectra recorded in the $\bar{\Gamma}\bar{K}$ (positive angles) and $\bar{\Gamma}\bar{K}'$ (negative angles) directions. A typical fitting with a set of Gaussians after linear background subtraction is shown for the experimental spectrum at $\theta=0°$. The intensities are normalized to the target current.

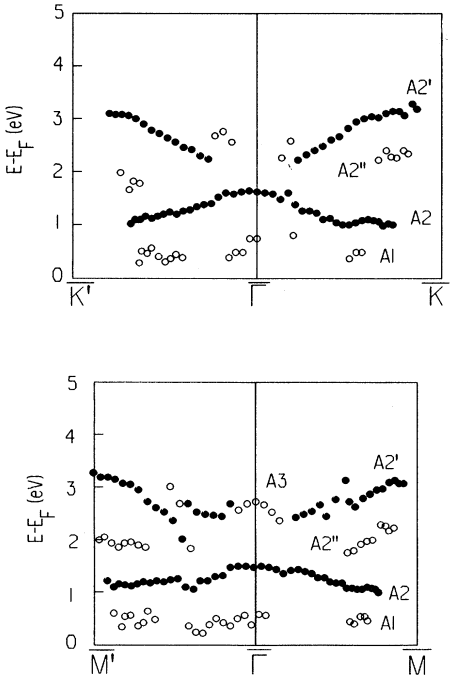

FIG. 4. Energy dispersion of the conduction-band states extracted from the measurements of Figs. 2 and 3, in the $\bar{M}'\bar{\Gamma}\bar{M}$ and $\bar{K}'\bar{\Gamma}\bar{K}$ directions, respectively.

B. Comparison with the theoretical predictions

The conduction-band structure of $2H$-MoS_2 has been calculated by several authors. For comparison with the experimental data, we have selected three different theoretical predictions which agree at least partially with the experimental data. These calculations are based on the augmented spherical wave[2] method (ASW), the augmented plane wave[1] (APW), and the layer method (LM).[16] As it is known, the experimentally measured $E(k_{\parallel})$ dispersion direction does not exactly match one symmetry direction of the calculation, like ΓM or AL (see Fig. 1), but rather corresponds to a complex path within the selected plane, like ΓMLA. Figures 5 and 6 reproduce part of the predicted conduction bands in the high symmetry directions of the three-dimensional BZ. The theoretical directions are indicated at the top of the plots, while the experimental orientations in the surface BZ are indicated at the bottom. The superposition is done by rigidly shifting the predicted bands in order to align the degenerate band A_2 at the Γ or A point.

All three different approaches predict that the A band is highly degenerate at the Γ point and is then split into several branches towards the zone boundaries. The predicted width in the ΓM direction is 3.5, 2.2, and 2.7 eV for ASW, APW, and LM, respectively, while it is 3.6, 3, and 4 eV in the ΓK direction. As can be seen in Figs. 5 and 6, these calculated bandwidths are always larger for ΓK and ΓM than for AH and AL. The measured width of the A_2 band including its split branches is 2.2 and 2.8 eV for $\bar{\Gamma}\bar{K}$ and $\bar{\Gamma}\bar{M}$, respectively. Considering that the experimental data correspond to projections in the ΓMLA and ΓKHA planes, an overall agreement is found. For instance, in Fig. 5(a), the experimental points in the $\bar{\Gamma}\bar{M}$ direction went out of the prediction for the

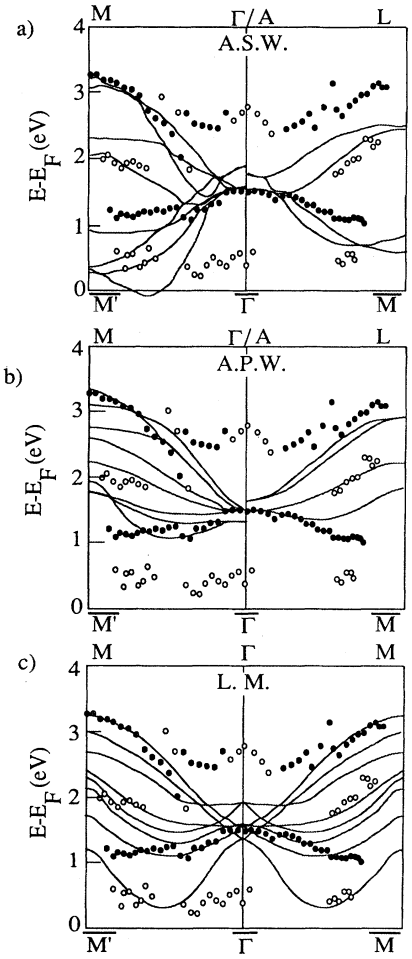

FIG. 5. Comparison between three different theoretical predictions (solid lines) and experimental data (dots) for the $\bar{M}'\bar{\Gamma}\bar{M}$ direction. Theoretical models: (a) augmented spherical waves; (b) augmented plane waves; and (c) layer method. Full dots indicate peaks which are well resolved experimentally, open symbols refer to shoulders.

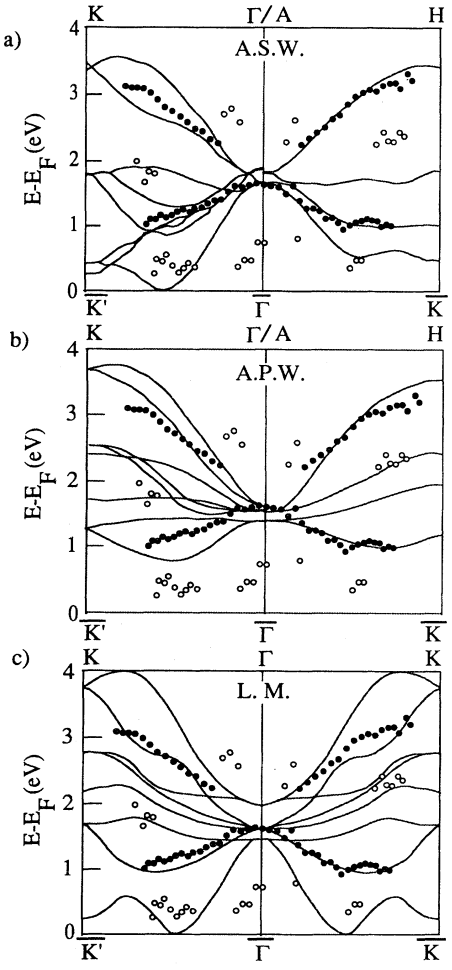

FIG. 6. Comparison between three different theoretical predictions (solid lines) and experimental data (dots) for the $\bar{K}'\bar{\Gamma}\bar{K}$ direction. Theoretical models: (a) augmented spherical waves (ASW) from Coehoorn, Haas, and de Groot (Ref. 3); (b) augmented plane waves (APW) from Mattheiss (Ref. 14); (c) layer method from Wood and Pendry (Ref. 16). Full dots indicate peaks which are well resolved experimentally, open symbols refer to shoulders.

AL direction, but they are well fitted by the projection of the ΓM prediction.

The lowest-energy branch A_1 is found around 0.4 eV above the Fermi level in both major directions. This dispersionless band is visible at all incident polar angles, but its intensity is higher for the k values for which a state is predicted in this low-energy range by the ASW and LM calculations. It is likely that this peak results from two contributions: one from the splitting of A_2 and the other one from a flat "impurity" band since cleavage of $2H$-MoS_2 usually produces a sulfur-rich surface.[6] In fact, a narrow occupied band situated just below the Fermi level is observed by photoemission in nearly all TX_2 layered compounds.[2,5] It is thus reasonable to argue that the observed A_1 peak reflects the corresponding antibonding counterpart of this state.

On the other hand, the presence of the A_3 band near the BZ center is more evident in $\bar{\Gamma}\bar{M}$ than in $\bar{\Gamma}\bar{K}$. This band qualitatively follows the same curvature as the uppermost branch expected from the ASW calculations but its absolute energy is significantly higher. This fact together with the intensity asymmetry will be explained by an initial-state effect to be discussed later.

C. Intensity asymmetries

Although the peak positions of all the observed bands symmetrically disperse in the $(E,k_{\parallel})$ space, an asymmetry of the intensities can be clearly seen in Figs. 2 and 3. For instance, A_2' is more intense for the positive polar angles in the $\bar{\Gamma}\bar{K}$ direction and a higher asymmetry of the peak intensities is observed in the $\bar{M}'\bar{\Gamma}\bar{M}$ direction. This asymmetry observed in the inverse photoemission spectra is not an artifact but stems from the intrinsic atomic structure of $2H$-MoS_2. Indeed, similar effects have already been reported on the photoemission spectra of the $1T$-$TiTe_2$ surface.[5]

A schematic view of a $2H$-MoS_2 crystal is displayed in Fig. 7, where the high symmetry directions of the BZ are indicated together with the atom positions in the real space. The cleaved basal surface is terminated by a hexagonal sulfur monolayer. The underlying Mo layer fills

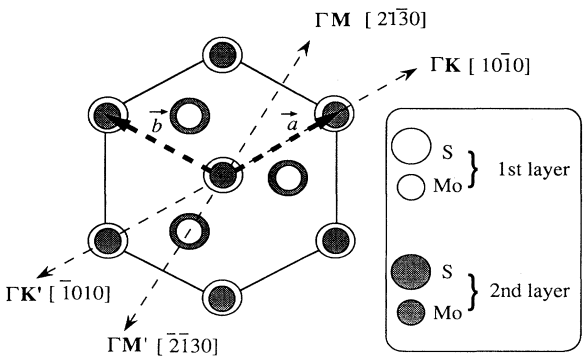

FIG. 7. Projection, along the c axis, of the atomic arrangement of the Mo and S atoms in two adjacent layers of $2H$-MoS_2 with the indication of the two basis vectors (**a** and **b**) in the direct space and the two high symmetry directions ($\bar{\Gamma}\bar{K}$ and $\bar{\Gamma}\bar{M}$) of the BZ.

only three hollow sites presented by the hexagonal network while the third sulfur layer matches exactly the first one. The unit cell contains another S-Mo-S sequence rotated by 60° and translated in order to find a molybdenum belonging to the second sandwich, right under the central sulfur atom of the first sandwich. In this sense, the atomic structure along [2$\bar{1}$30] and [$\bar{2}$ $\bar{1}$30], corresponding to $\bar{\Gamma}\bar{M}$ and $\bar{\Gamma}\bar{M}'$ in the reciprocal space, is not identical. A similar structural asymmetry can be found for the H/Si(111) surface. Instead of p-d hybridization, H/Si(111) is an s-p coupled system on which both intensity and dispersion asymmetries have been reported by KRIPES (Ref. 21) and ARPES.[22]

In the case of TX_2, the intensity asymmetry is well known in the valence-band dispersion experiments. Moreover, recent scanning tunneling microscopy (STM) results on MoS_2 have shown that the lowest conduction-band states exhibit node planes through the S atom and a strongest tunneling current intensity is obtained over the subsurface Mo sites when the distance between the tip and sample is large.[23] This implies that there is a long lobe of hybridized p-d antibonding band located near the Mo sublayer pointing out the first sulfur layer, which is clearly asymmetric along the $\bar{M}'\bar{\Gamma}\bar{M}$ direction. On the contrary, it should be symmetric along $\bar{\Gamma}\bar{K}$. Nevertheless, as described above, we have observed some intensity asymmetry in this direction, which could be explained by the sample roughness resulting from the cleavage procedure and/or by a slight misalignment of the azimuth ϕ. Taking these facts into account, we can understand why the contribution of these asymmetric components becomes more and more important near the boundary of the BZ.

The intensity asymmetry along the $\bar{M}'\bar{\Gamma}\bar{M}$ direction is also observed in the target current spectra. As mentioned above, the target current is always recorded during the KRIPES measurements and used to normalize the photon counts. On the other hand, as it has been demonstrated on graphite surfaces, the modulation of the TCS reflects the band structure of the unoccupied states above the vacuum level since the other effects can merely cause a continuous background.[24] Low-energy electron transmission (LEET) spectra, which can provide information similar to that provided by TCS, have recently been measured by Ueno *et al.*[25] on an *in situ* cleaved MoS_2 surface. Comparing with our angle-resolved TCS, their LEET spectrum is similar to the TCS spectra recorded near the $\bar{\Gamma}$ point.

The whole set of TCS data is plotted in Fig. 8, where the energy reference is the Fermi level. Several features can be identified as C, A^*, and B^* bands. All these bands are symmetrically distributed with respect to the $\bar{\Gamma}$ point in $\bar{K}'\bar{\Gamma}\bar{K}$ direction while only C is symmetric for the $\bar{M}'\bar{\Gamma}\bar{M}$ direction. Due to the fact that there is usually a smooth background underpinning the current modulation, it is difficult to follow all the peak positions exactly in order to provide a band dispersion.

As it is commonly accepted, the modulation of the unoccupied states can be emphasized by using the negative second derivative ($-d^2I/dE^2$) of the TCS data. This is illustrated for $\theta=0°$ in curve (c) of Fig. 9. Compared

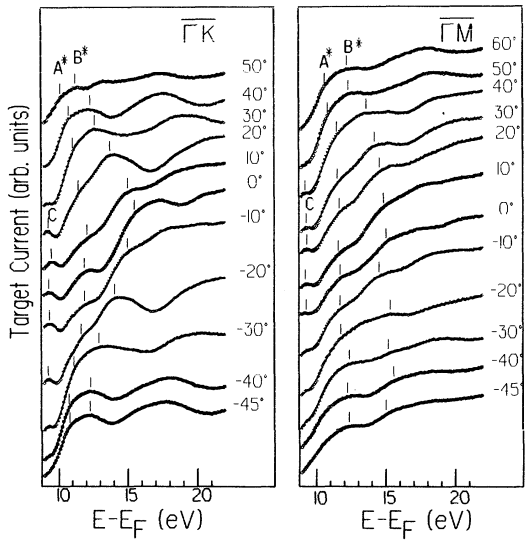

FIG. 8. Target current spectra recorded on $2H$-MoS_2 during the KRIPES measurements along the two principal directions $\bar{\Gamma}\bar{K}$ and $\bar{\Gamma}\bar{M}$ of the BZ.

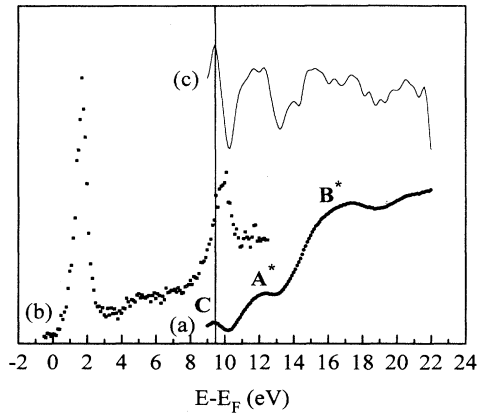

FIG. 9. (a) Target current spectrum corresponding to the KRIPES spectrum (b) measured on $2H$-MoS_2 at $\bar{\Gamma}$; (c) negative second derivative of the target current spectrum (b).

with the raw TCS data (a), the derivative (c) provides a better determination of the three bands and reveals some additional fine structures which are not discernible in the current spectrum. However, care should be taken when interpreting these fine structures because the second derivative of one peak usually produces more than one peak. This is the reason why we will not use them to map the bands. Still, useful information can be directly extracted from our TCS spectra: the sharp C band is only present near the BZ center and does not disperse significantly, while the very broad A^* and B^* bands are dispersive.

D. Initial-state effects

Since the intensity of the photon spectrum is determined by the joint density of states while the TCS only provide the initial-state modulation, we can expect that some of the conduction bands can be observed in both techniques in the common energy range. For this reason, the corresponding KRIPES spectrum is plotted in Fig. 9(b) together with the TCS (a) and its negative second derivative (c). One can immediately find that the same conduction-band state C is present at 9.5 eV in all spectra. In the current spectrum, it represents a direct matching of the incident electron wave with the eigenwave function of this state, while it appears in the photon spectrum as the final state corresponding to the radiative transition from the initial state situated 9.5 eV higher. Because there is a dip at 19 eV above the Fermi level, the peak C observed in the photon spectrum is really a final-state effect. In the meantime, we recognize that this peak is observed only near the center of the BZ for both cases ($\bar{\Gamma}\bar{K}$ and $\bar{\Gamma}\bar{M}$), which implies that the lobe of the wave function of this state is oriented perpendicularly to the surface, and suggests that it most probably originates from the sulfur p_z states.

In order to show more clearly the initial-state effects on the KRIPES spectrum, we have rigidly shifted the TCS and its corresponding second derivative by the detected photon energy (9.5 eV) towards lower energy, as shown in Fig. 10. This brings three interesting considerations. (1) The high intensity of the A band can be explained by the resonant transition between the A^* and A bands. As the width of the A^* band is much larger, the splitting and dispersion seen in Figs. 2–4 originate mainly from the A band. (2) The asymmetry of the observed KRIPES intensities can be partially attributed to an initial-state effect. As the shape of the A^* band is determined by the TCS, an asymmetry observed in the current spectra shall induce an equivalent asymmetry in the density of states. (3) The A_3 peak intensity observed in KRIPES can be attributed to an initial-state effect due to a higher density of states appearing in the A^* band. As it has been men-

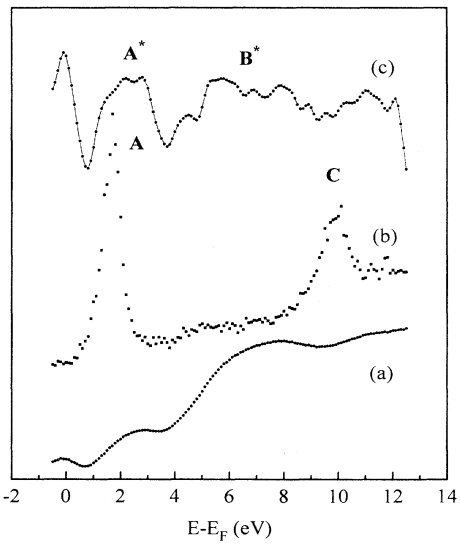

FIG. 10. Same spectra as Fig. 9, with (a) current and (c) negative second derivative both shifted by the isochromatic photon energy of 9.5 eV.

tioned, the dispersion of the A_3 band follows the same curvature as the predicted A_2' branch, it can be understood that A_3 is in the tail of the A_2 band but enhanced by high initial-state density. The resonance disappears when the A^* band disperses towards lower energy while $k_\parallel$ increases, which explains why A_3 only appears near the $\overline{\Gamma}$ point.

IV. CONCLUSION

The conduction band of $2H$-MoS_2 has been investigated by $k_\parallel$-resolved inverse photoemission along two main symmetry directions, $\overline{M}'\overline{\Gamma}\,\overline{M}$ and $\overline{K}'\overline{\Gamma}\,\overline{K}$. The dispersion of the lowest bands (A) has been compared with three different calculations and a good general agreement has been found with the projected band structures. The lowest-energy state, not predicted by the theoretical approaches has been tentatively explained by an impurity band. On the other hand, the origin of the intensity asymmetry of the KRIPES spectra along $\overline{M}'\overline{\Gamma}\,\overline{M}$ has been attributed to the asymmetrical atomic structure of the sample. Finally, the same conduction-band state situated around 9.5 eV above the Fermi level is detected as an initial state in the TCS measurement and as a final state in the photon spectra.

ACKNOWLEDGMENTS

We thank G. Treglia for helpful discussions. L.-M.Y. acknowledges the financial support from the interuniversity research program on "Materials Characterization" initiated by the Belgian State Prime Minister's Office (federal services for scientific, technical, and cultural affairs). The "Groupe de Physique des Etats Condensés" is Unité de Recherches Associée au CNRS No. 783.

[1]L. F. Mattheiss, Phys. Rev. B **8**, 3719 (1973).
[2]R. Coehoorn, C. Haas, J. Dijkstra, C. J. F. Flipse, R. A. de Groot, and A. Wold, Phys. Rev. B **35**, 6195 (1987).
[3]R. Coehoorn, C. Haas, and R. A. de Groot, Phys. Rev. B **35**, 6203 (1987).
[4]K. Fives, I. T. McGovern, R. McGrath, R. Cimino, G. Hugues, A. McKinley, and G. Thornton, J. Phys. Condens. Matter **4**, 5639 (1992).
[5]D. K. G. de Boer, C. F. van Bruggen, G. W. Bus, R. Coehoorn, C. Haas, G. A. Sawatzky, H. W. Myron, D. Norman, and H. Padmore, Phys. Rev. B **29**, 6797 (1984).
[6]J. R. Lince, S. V. Didziulis, and J. A. Yarmoff, Phys. Rev. B **43**, 4641 (1991).
[7]I. Abbati, L. Braicovich, C. Carbone, J. Nogami, J. J. Yeh, I. Lindau, and U. del Pennino, Phys. Rev. B **32**, 5459 (1985).
[8]I. T. Govern, K. D. Childs, H. M. Clearfield, and R. H. Williams, J. Phys. C **14**, L243 (1981).
[9]M. Sancrotti, L. Braicovich, C. Chemelli, and G. Trezzi, Solid State Commun. **66**, 593 (1988).
[10]A. Serpi, Phys. Status Solidi A **133**, K73 (1992).
[11]J. C. McMenamin and W. E. Spicer, Phys. Rev. B **16**, 5474 (1977).
[12]S. Hosoki, S. Hosaka, and T. Hasegawa, Appl. Surf. Sci. **60/61**, 643 (1992).
[13]M. Sakurai, H. Tada, K. Saiki, A. Koma, H. Funasaka, and Y. Kishimoto, Chem. Phys. Lett. **208**, 425 (1993).
[14]L. F. Mattheiss, Phys. Lett. **30**, 784 (1973).
[15]D. W. Bullett, J. Phys. C **11**, 4501 (1978).
[16]K. Wood and J. B. Pendry, Phys. Lett. **31**, 1400 (1973).
[17]R. V. Kasowski, Phys. Lett. **30**, 1175 (1973).
[18]S. P. Hind and P. E. Lee, J. Phys. C **13**, 349 (1980).
[19]A. R. Williams, J. Kübler, and C. D. Gelatt, Jr., Phys. Rev. B **19**, 6094 (1979).
[20]J-L. Calais, Adv. Phys. **26**, 847 (1977).
[21]S. Bouzidi, F. Coletti, J.-M. Debever, P. A. Thiry, P. Dumas, and Y. Chabal, Phys. Rev. B **45**, 1187 (1992).
[22]Y. He *et al.* (private communication).
[23]A. J. Fisher and P. E. Blöchl, Phys. Rev. Lett. **70**, 3263 (1993).
[24]I. Schäfer, M. Schlüter, and M. Skibowski, Phys. Rev. B **34**, 14 (1987), and references therein.
[25]N. Ueno, K. Susuki, M. Momose, M. Kushida, and K. Sugita, Jpn. J. Appl. Phys. **33**, 319 (1994).